



Cite as
Nano-Micro Lett.
(2021) 13:107

Received: 22 December 2020
Accepted: 25 February 2021
Published online: 9 April 2021
© The Author(s) 2021

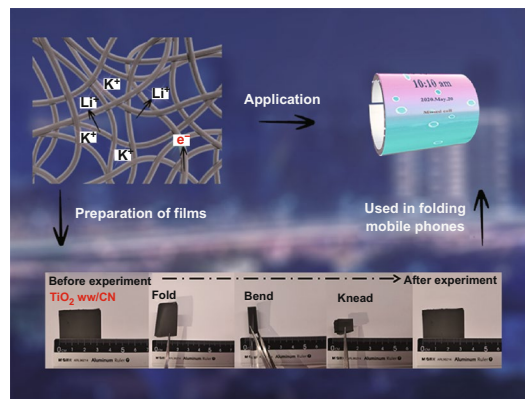
Wire-in-Wire TiO₂/C Nanofibers Free-Standing Anodes for Li-Ion and K-Ion Batteries with Long Cycling Stability and High Capacity

Die Su¹, Yi Pei², Li Liu¹ ✉, Zhixiao Liu³ ✉, Junfang Liu¹, Min Yang¹, Jiaying Wen¹, Jing Dai¹, Huiqiu Deng⁴, Guozhong Cao² ✉

HIGHLIGHTS

- The unique wire-in-wire structure endows TiO₂/C nanofibers film with superior mechanical flexibility.
- The wire-in-wire TiO₂/C nanofibers (TiO₂ ww/CN) film shows outstanding electrochemical performances as free-standing anodes for Li/K-ion batteries and full cells.
- The TiO₂ ww/CN film shows an extremely high pseudocapacitance contribution ratio in K-ion batteries.

ABSTRACT Wearable and portable mobile phones play a critical role in the market, and one of the key technologies is the flexible electrode with high specific capacity and excellent mechanical flexibility. Herein, a wire-in-wire TiO₂/C nanofibers (TiO₂ ww/CN) film is synthesized via electrospinning with selenium as a structural inducer. The interconnected carbon network and unique wire-in-wire nanostructure cannot only improve electronic conductivity and induce effective charge transports, but also bring a superior mechanic flexibility. Ultimately, TiO₂ ww/CN film shows outstanding electrochemical performance as free-standing electrodes in Li/K ion batteries. It shows a discharge capacity as high as 303 mAh g⁻¹ at 5 A g⁻¹ after 6000 cycles in Li half-cells, and the unique structure is well-reserved after long-term cycling. Moreover, even TiO₂ has a large diffusion barrier of K⁺, TiO₂ ww/CN film demonstrates excellent performance (259 mAh g⁻¹ at 0.05 A g⁻¹ after 1000 cycles) in K half-cells owing to extraordinary pseudocapacitive contribution. The Li/K full cells consisted of TiO₂ ww/CN film anode and LiFePO₄/Perylene-3,4,9,10-tetracarboxylic dianhydride cathode possess outstanding cycling stability and demonstrate practical application from lighting at least 19 LEDs. It is, therefore, expected that this material will find broad applications in portable and wearable Li/K-ion batteries.



KEYWORDS Free-standing TiO₂/C nanofiber; Li-ion battery; K-ion battery; First-principles calculation; Full cells

✉ Li Liu, liulili1203@126.com; Zhixiao Liu, zxliu@hnu.edu.cn; Guozhong Cao, gzcao@uw.edu

¹ National Base for International Science and Technology Cooperation, National Local Joint Engineering Laboratory for Key Materials of New Energy Storage Battery, Hunan Province Key Laboratory of Electrochemical Energy Storage and Conversion, School of Chemistry, Xiangtan University, Xiangtan 411105, People's Republic of China

² Department of Materials Science and Engineering, University of Washington, Seattle, WA 98195-2120, USA

³ College of Materials Science and Engineering, Hunan University, Changsha 410082, People's Republic of China

⁴ School of Physics and Electronics, Hunan University, Changsha 410082, People's Republic of China



1 Introduction

With the development of flexible electronic devices or wearable devices, the studies for flexible energy-storage devices are becoming increasingly attractive [1, 2]. As one of the most efficient energy storage devices, flexible Li-ion batteries (LIBs) gradually become all-important in the field of energy storage. Recently, K-ion batteries (KIBs) have attracted masses of attention because of their abundant raw materials in natural resources, similar working mechanisms, and approximate standard reduction potential (lithium: -3.04 V vs. E^0 , potassium: -2.93 V vs. E^0) compared with LIBs [3–5]. The flexible electrodes with high-performance are essential for the applications of flexible advanced secondary batteries.

Binding-free and free-standing anode materials for LIBs, including layered transition metal oxides and sulfides [6, 7], have made great breakthroughs in flexible and wearable devices and other small portable electronic products. However, binding-free and free-standing anode materials for KIBs principally focus on red phosphorus or black phosphorus-doped carbon [8, 9], the reports about oxides or sulfides as free-standing anode materials are few. Titanium dioxide (TiO_2) has distinct advantages in battery materials because of its wonderful natural abundance, low cost, and stable crystal structure. Thus, it has been extensively reported as anode electrode materials for LIBs and commonly exhibited long cycling stability due to small changes in volume size during repeated insertion/extraction of the crystal structure [10–13]. Nevertheless, theoretical specific capacity of TiO_2 is 336 mAh g^{-1} based on inserting 1 mol Li per molecule, its actual specific capacity is usually not satisfied and the Li insertion amount is frequently limited below 0.5 mol [14]. Although TiO_2 layer on N-doped carbon foams [15], EOG/ TiO_2 (B) nanosheets [16], and N-doped TiO_2 /rGO [17] have been reported as free-standing anodes for LIBs, their specific capacity and flexibility have a lot of room for improvement.

Making every effort to investigate, there are only three reports about TiO_2 as anodes for KIBs. Hierarchical TiO_2 -C micro-tubes [18], lepidocrocite-type layered TiO_2 [19], and MXene-derived TiO_2 /RGO [20] have been synthesized and studied as anode materials for KIBs. It is noteworthy that free-standing TiO_2 anode in K-ions battery has not been reported as we know. This is a great challenge

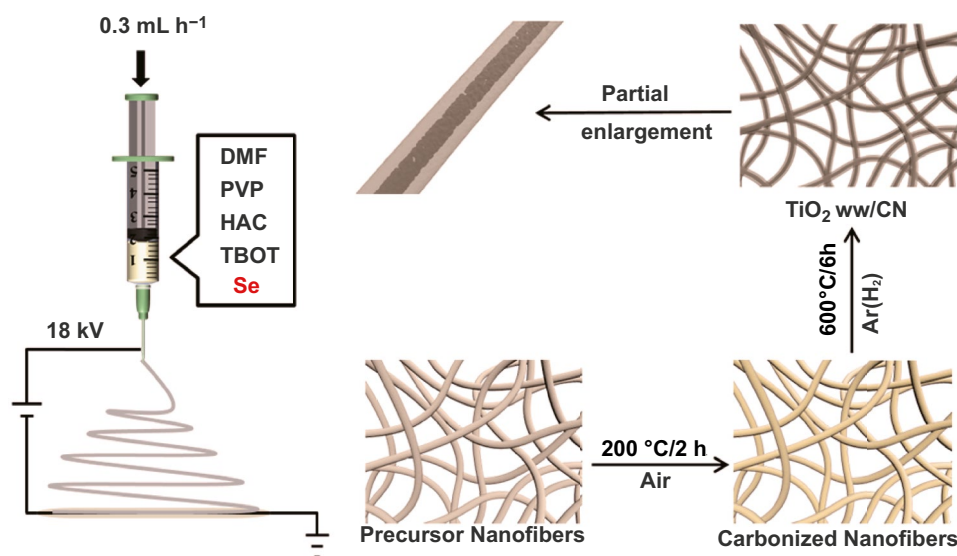
to achieve high mechanical flexibility between TiO_2 nanoparticles and carbon matrix materials. Herein, using selenium as a structural inducer, wire-in-wire TiO_2 /C nanofibers (denoted as TiO_2 ww/CN) film has been synthesized via electrospinning. Without a traditional coating process, it possesses the characteristics of long cycle life and high capacity as independent electrode anodes for Li/K half cells and full cells. Excellent lithium and potassium storage performance and strong mechanical flexibility make it become a potential flexible anode candidate.

2 Experimental Section

2.1 Synthetic Section

All the reagents, including tetra-*n*-butyl titanate (TBOT, $\text{C}_{16}\text{H}_{36}\text{O}_4\text{Ti}$, Kermel), *N,N*-dimethylformamide (DMF, $\text{C}_3\text{H}_7\text{NO}$, Sinopharm, China), polyvinylpyrrolidone (PVP, $(\text{C}_6\text{H}_9\text{NO})_n$, MW = 1,300,000, Alfa Aesar), commercial LiFePO_4 (LFP, BTR New Material Group Co., Ltd, China), perylene-3,4,9,10-tetracarboxylic dianhydride (PTCDA, Aladdin, China), glacial acetic acid (HAC, CH_3COOH , Kermel), and selenium powder (Se, Macklin, 200 mesh) are analytically pure grade and used directly.

The synthetic route is shown in Scheme 1. First, 0.8 g PVP was dissolved in 9 mL DMF via stirring to obtain a clear transparent solution. Then, 1.5 mL CH_3COOH and 2 mL TBOT were added to the solution slowly. After 10 min, 0.48 g selenium powder was added to the above solution with stirring at 60 °C for 24 h and ultrasonic dispersion for 1 h. The digital photo of the precursor solution (including DMF, PVP, TBOT, HAC, and Se) shown in Fig. S1a confirmed the complete dissolution of Se powder in the colloids of DMF and PVP, while the compared one without PVP showed considerable undissolved Se powder in Fig. S1b. The precursor solution was spun under 18 kV to obtain the precursor nanofibers film. Then, the precursor nanofiber film was stabilized in air at 200 °C/2 h. In the end, the TiO_2 ww/CN film was obtained by annealing the stabilized nanofibers film in Ar (H_2) (95:5) atmosphere at 600 °C/6 h. The thickness of the TiO_2 ww/CN film is about 0.083 mm (as shown in Fig. S1c). For comparative study, common TiO_2 /C nanofibers (TiO_2 /CN) film was obtained from the precursor solution without Se adding by



Scheme 1 Schematics illustration of the process used to produce the TiO_2 ww/CN film

the above procedure. Besides, the PTCDA used as cathode materials in K full cell (KFC) was pretreated by annealing at $450\text{ }^\circ\text{C}$ for 4 h in Ar [5].

2.2 Structure and Morphology Characterization

The crystal structure of all samples was characterized by X-ray diffraction (XRD, Rigaku, Ultima IV with D/teX Ultra with $\text{Cu-K}\alpha$ radiation) at a scan rate of 5° min^{-1} . The Raman spectra of the sample were characterized by the microlaser Raman spectrometer (Raman, Renishaw inVia, plc England). The elemental distribution on the surface of the nanofibers was characterized by X-ray photoelectron spectroscopy (XPS, Kratos Axis Ultra DLD, Japan) ($h\nu = 1486.6$) using a Kratos Axis Ultra DLD spectrometer of a monochromatic $\text{Al K}\alpha$ X-ray source. The content of the carbon and selenium was measured by an elemental analyzer (TG, NETZSCH STA 409 PC/PG, Germany). The morphology and microscopic structure of the product were presented by field emission scanning electron microscopy (FE-SEM, Hitachi, SU8010, Japan) and transmission electron microscopy (FE-TEM, FEI-Tecnai G2 TF20, America). The corresponding element mapping was performed by the high-angle annular dark-field (HAADF) and selected area electron diffraction (SAED). The specific surface area and the porous structure were calculated by a specific surface and aperture analyzer

(BET, Quadrasorb SI-3MP, USA). And the pore size distribution was estimated with BJH method.

2.3 Electrochemical Tests

Without using any binder, conductive additive, and metal current collector, the obtained samples were punched to discs with a diameter of 10 mm and directly applied as working electrodes. And the area loading of active materials in the electrodes is about 0.7 mg cm^{-2} . The slurry is composed of the 70 wt% of the active substance (LFP or PTCDA), 20 wt% of carbon black, 10 wt% of polyvinylidene fluoride, and appropriate *N*-methyl-2-pyrrolidone is pasted on aluminum foil to form cathodes for Li/K full cells. The mass loading of active materials for LFP electrode is about 0.77 mg cm^{-2} and PTCDA electrode is about 1.4 mg cm^{-2} . The Li half cell (LHC) was fabricated by sandwiching a separator (Whatman GF/A) between lithium metal and working electrode into CR2025 coin cell, and the 1.0 M LiPF_6 with ethylene carbonate/dimethyl carbonate (EC/DMC) (1:1 vol %) was employed as the electrolyte. The lithium metal was replaced by the LFP cathode to assemble Li full cell (LFC). The CR2032 K half cell (KHC) was assembled using a working electrode, potassium metal, glass fiber membrane (Whatman GF/D) as a separator, and 1.0 M KFSI in ethylene carbonate/dimethyl carbonate (EC/

DMC) (1:1 vol%) as an electrolyte. The potassium metal was replaced by the PTCDA cathode to fabricate KFC. To ensure the cell balance, setting the weight ratio of cathode to anode active material is about 2:1 in LFCs and 1.1:1 in KFCs. All cells were assembled in the glovebox that both moisture and oxygen concentration were less than 0.1 ppm. The Neware BT3008W battery test system (China) was measured to test the constant current discharge/charge process. The Chenhua CHI660E Analyzer (China) was performed on cyclic voltammetry (CV) and A.C. impedance (frequency range: 0.01 Hz to 100 kHz; amplitude: 5 mV).

2.4 Computational Details

All first-principles simulations (DFTs) are performed by the Vienna Ab-initio Simulation Package [21, 22]. The projector augmented-wave (PAW) method [23] was used to demonstrate the ion–electron interactions. The Perdew–Burke–Ernzerhof (PBE) functional [24] was employed for describing the electron–electron exchange correlations. The onsite Coulomb interaction is considered in the present study to describe the localized d electrons of transition metals, and the U_{eff} parameters were set to 2 eV. In all DFT simulation, making the cutoff energy of the plane wave basis sets equals 400 eV, and the density of k points equals to 0.15 \AA^{-1} . The residual force for optimizing atom positions was less than 0.02 eV \AA^{-1} .

3 Results and Discussion

3.1 Sample Characterization

The XRD patterns show crystallographic information in Fig. 1a. The diffraction peaks of both TiO_2/CN and TiO_2 ww/CN are fitted well with the anatase (JCPDS No. 21-1272) without impure phases, indicating that pure-phase TiO_2 is successfully prepared by electrospinning method. The FE-SEM image shows that the precursor nanofibers of the TiO_2 ww/CN (Fig. S2a) have a large length-diameter ratio with diameters of about 200 nm. However, the diameters of the carbonized nanofibers (Fig. 1b) are significantly reduced to 160 nm. The TiO_2/CN film and its precursor show similar morphologies with that of TiO_2 ww/CN film and its precursor (Fig. S2b, c). To further investigate the morphology of TiO_2 ww/CN film, the FE-SEM image of the

fractured cross section of nanofibers is shown in Fig. 1c, indicating the nanofibers are solid. As shown in the TEM image (Fig. S3a), TiO_2 nanoparticles in TiO_2/CN have been uniformly embedded into the carbon nanofibers matrix. The TiO_2 nanoparticles have diameters of ~ 6 nm and the lattice fringe of 3.5 \AA from the HRTEM image (Fig. S3b) could be assigned to the (101) planes of anatase-phase TiO_2 . Meanwhile, the corresponded fast Fourier transform (FFT) pattern shows one set of polycrystalline rings that match well with the layer distance of (101) planes. The EDX element mapping image shown in Fig. S3c has indicated the even dispersion of C, Ti, and O within nanofiber, suggesting no element segregation in TiO_2/CN . The TEM images of TiO_2 ww/CN are shown in Fig. 1d, e. Despite a similar one-dimensional morphology (diameter of ~ 160 nm) of TiO_2 ww/CN with that of TiO_2/CN , the core of TiO_2 ww/CN shows much higher contrast than that of the edge region, suggesting that TiO_2 is probably aggregated in the core region and form a unique wire-in-wire nanostructure. The phase constitution in the interior region of TiO_2 ww/CN is further investigated through HRTEM analysis (Fig. 1f), from which the lattice fringes with an interplanar spacing of 3.5 \AA is consistent with the (101) plane of anatase TiO_2 , and the rings in FFT pattern are attributed to (101). The EDX element mapping images (Fig. 1g) confirm that the C, Ti, O elements are distributed in the whole nanofiber. To confirm the distribution of C and Ti elements, the TEM–EDX mapping line scan (Figure S4) is carried out. According to the scanning route in Fig. S4a, the EDX lines of the atomic ratio of the elements (C and Ti) were shown in Fig. S4b. It was observed that the C element increases gradually from inside to outside, while Ti element decreases gradually from inside to outside. This further supports the unique wire-in-wire nanostructure. To further investigate the inner structure of TiO_2 ww/CN film, it was calcined in air at $400 \text{ }^\circ\text{C}$ for 2 h to remove the carbon matrix. The digital photo and TEM results of the residues are shown in Fig. S5. The black TiO_2 ww/CN film turns into a white TiO_2 film after burning in air (Fig. S5a), fortunately, the film structure is still intact. FE-TEM images in Fig. S5b, c demonstrate that the nanofibers (~ 60 nm) are composed of nanoparticles with diameters of about 6 nm. The interplanar spacing of HRTEM image (Fig. S5d) and SAED pattern (Fig. S5e) is all corresponding to (101) planes of anatase TiO_2 phase (JCPDS No. 21-1272). EDX elemental mapping image shown in Fig. S5f indicates the nanowires are made up of Ti, O, and C elements. Figure 1h

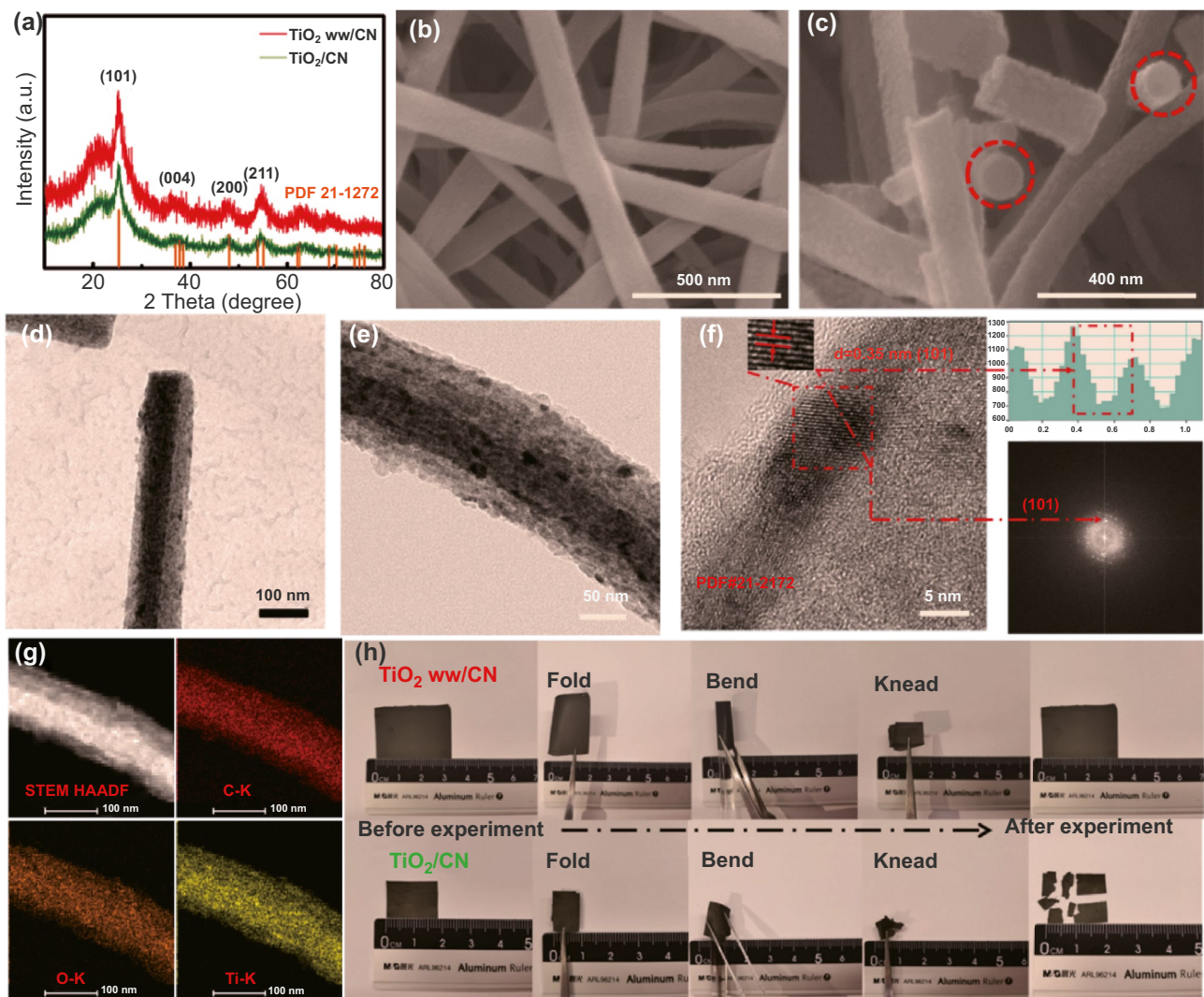


Fig. 1 a XRD patterns of TiO₂ ww/CN and TiO₂/CN; FE-SEM images of b TiO₂ ww/CN film and c the fracture cross section nanofibers for TiO₂ ww/CN; d, e FE-TEM images, f HRTEM images, and g EDX elemental mapping images of C, O, Ti of TiO₂ ww/CN; h the digital photos of TiO₂ ww/CN film and TiO₂/CN film before and after the experiment of completely folded, bent and kneaded in sequence

shows the digital photos of TiO₂ ww/CN film and TiO₂/CN film before and after the experiment of completely folded, bent, and kneaded in sequence. The TiO₂/CN film is broken and couldn't recover after the experiment, while the original state TiO₂ ww/CN film is well-reserved, demonstrating the remarkable mechanical flexibility of TiO₂ ww/CN film. More detailed information on the mechanical flexibility of TiO₂/CN film and TiO₂ ww/CN film can be seen in Video S1. It's worth noting that the TiO₂ ww/CN film is intact after bending, folding, and kneading sequentially.

Therein, it can conclude that the addition of Se powder has induced the formation of specific wire-in-wire configuration in TiO₂ ww/CN with superior mechanical performance.

Even that the crucial role of Se powder could be confirmed by comparing the phase distribution of TiO₂ ww/CN and TiO₂/CN, the mechanism is still unclear. In consequence, further comparisons are designed and carried out on all the precursor, intermediate and as-synthesized products. The element composition and corresponding chemical states of TiO₂ ww/CN and TiO₂/CN were explored by XPS. The survey spectra in Fig. 2a demonstrate that two samples have the same signal peaks of Ti, C, and O elements which are consistent with EDS from FE-TEM (Fig. S6). No signal of Se is detected in the spectra of TiO₂ ww/CN, suggesting that Se is thoroughly evaporated. To further probe the electronic states of Ti and C, high-resolution C 1s and Ti

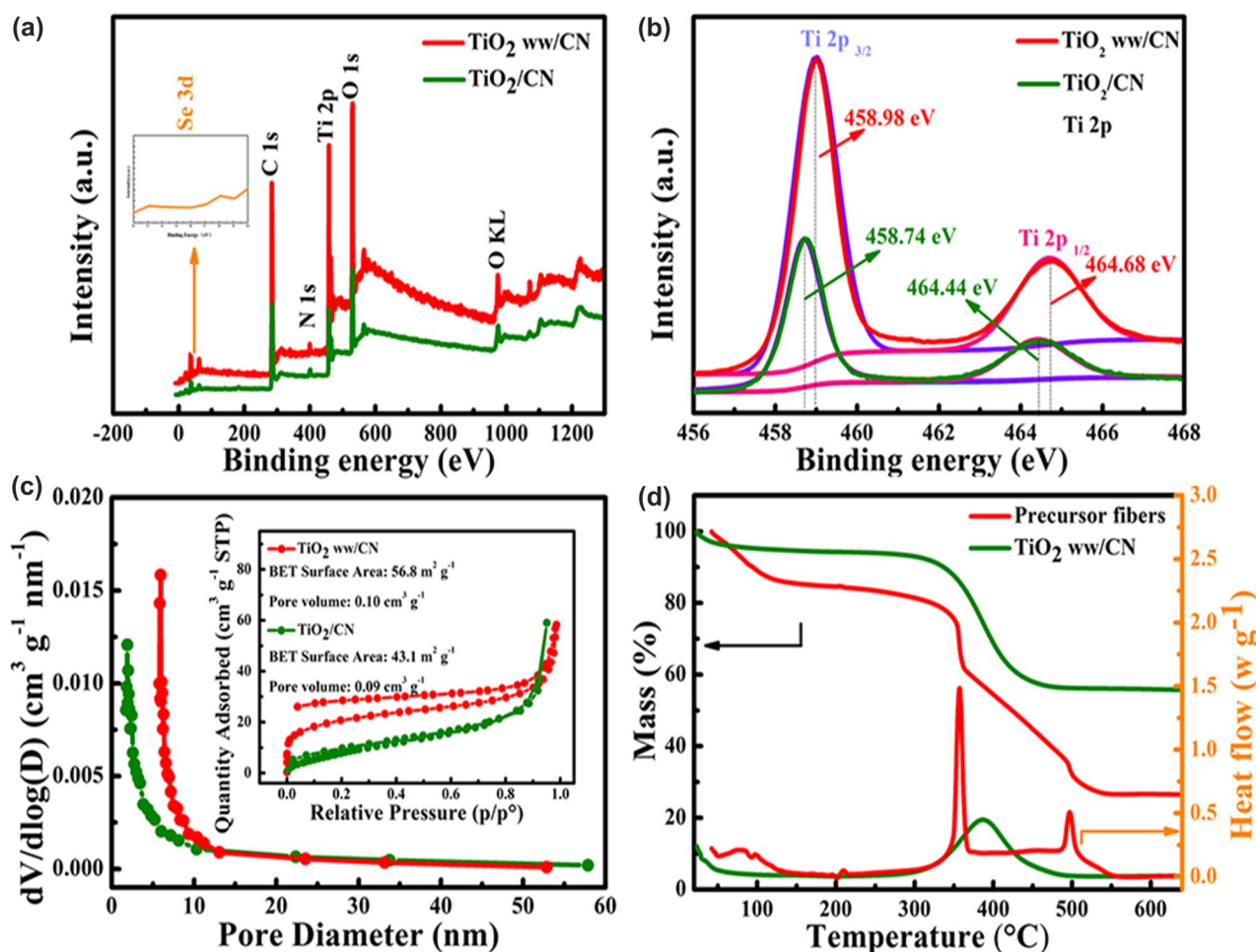


Fig. 2 **a** XPS survey spectra, **b** the high-resolution Ti 2p of TiO₂ ww/CN and TiO₂/CN; **c** the pore volume distribution of both TiO₂ ww/CN and TiO₂/CN, corresponding N₂ adsorption/desorption curves (inserted image); **d** TG and DTA of TiO₂ ww/CN and precursor fibers in air at a rate of 5 °C min⁻¹

2p spectra are shown in Figs. S7 and 2b, respectively. Both TiO₂/CN and TiO₂ ww/CN demonstrate three conditions of C: C–C bond (284.80 eV), C–O bond (286.20 eV), and O–C=O bond (288.00 eV), and the main peak at 284.80 eV is attributed to unoxidized carbon, while the signal from 286.20 and 288.00 eV is traced from incomplete carbonization of PVP [25–28]. It can be observed in Fig. 2b that Ti 2p spectra of TiO₂ ww/CN are slightly different from TiO₂/CN. Two peaks locating in 458.74 and 464.44 eV for TiO₂/CN correspond to the Ti 2p_{3/2} and Ti 2p_{1/2} peaks of TiO₂, respectively. For TiO₂ ww/CN, these two peaks shift to 458.98 and 464.68 eV, respectively. The higher binding energy of Ti 2p for TiO₂ ww/CN is maybe concerned with the oxygen vacancies caused by the addition of structural

inducers[29]. Consequently, XPS measurements are carried out on the precursor solution to probe the chemical state change of Se upon calcination (Fig. S8). The Se 3d spectra obtained from the precursor solution showed a characterization peak at 53.90 eV, which is corresponded to Se⁰⁺ in elementary Se [30, 31]. Therefore, interior nanofibers and exterior nanofibers of TiO₂ ww/CN are comprised of TiO₂ and carbon matrix. The formation of a unique hierarchical structure may be attributed to the selenium-gradient evaporation caused by annealing. As shown in Figs. S1 and S9 (FE-SEM image EDAX of the precursor nanofibers of TiO₂ ww/CN), the selenium element is distributed uniformly in the precursor solution and precursor nanofibers after electrospinning. However, because of the low sublimation temperature

of Se, the outer layer of the fibers may be enriched with selenium with the increase in temperature during annealing. Contrarily, titanium oxides would be concentrated on the inner layer of the fiber because of their high thermal stability. Then, the embedded selenium in exterior gradually sublime with the temperature rises during annealing to form the unique wire-in-wire structure.

The N_2 adsorption/desorption curves and corresponding pore volume distribution of both TiO_2 ww/CN and TiO_2 /CN are shown in Fig. 2c to compare the surface condition. The specific surface area value of TiO_2 ww/CN is $56.8 \text{ m}^2 \text{ g}^{-1}$ with the pore volume value of $0.10 \text{ cm}^3 \text{ g}^{-1}$, which is higher than that of TiO_2 /CN ($43.1 \text{ m}^2 \text{ g}^{-1}$, $0.09 \text{ cm}^3 \text{ g}^{-1}$). This larger specific surface area and pore volume are probably traced from the formation of the void by the evaporation of selenium. Besides, it was observed from the pore volume distribution that TiO_2 /CN have micropores, while TiO_2 ww/CN has mesopores and micropores. The TG-DTA curves of both TiO_2 ww/CN and its precursor fibers in air are shown in Fig. 2d. The TG curve of precursor fibers shows two obvious stages of weight loss, corresponding to two heat flow peaks at 350 and 500 °C in the DTA curves, respectively. The weight losses at about 350 and 500 °C could be attributed to the decomposition of PVP and the sublimation of Se, respectively. Thus, selenium could be expected to be completely evaporated during the annealing process at 600 °C. The TG-DSC curves of TiO_2 ww/CN and TiO_2 /CN in air are shown in Fig. S10. Both samples showed a similar weight loss process, within which the region before 200 °C is attributed from the loss of physically adsorbed water, and the weight loss between 300 and 500 °C with a heat flow signal peak at about 400 °C in the DSC curve caused by the burning of carbon in air. Thus, it can be calculated the carbon contents of those two samples are very close which are about 40.3% and 40.0%, respectively. The Raman spectra shown in Fig. S11 exhibited a similar intensity ratio of D band peak and G band peak (I_D/I_G) in TiO_2 ww/CN and TiO_2 /CN (0.856), implying the comparable degree of ordering for carbon in TiO_2 ww/CN and TiO_2 /CN.

3.2 Electrochemical Evaluation in LHCs and Full Cells

Figure 3a compares the rate performance between the TiO_2 ww/CN electrode and the TiO_2 /CN electrode. At 0.05, 0.1, 0.2, 0.4, 0.6, and 0.8 $A \text{ g}^{-1}$, the TiO_2 ww/CN electrode can reach

the capacities of 753, 574, 381, 300, 265, and 225 mAh g^{-1} , respectively, which are much higher than those of TiO_2 /CN electrode. Even at 1, 3, and return to 0.05 $A \text{ g}^{-1}$, the TiO_2 ww/CN electrode delivers the discharge specific capacities of 192, 149, and 750 mAh g^{-1} , respectively. The cycling performance of the TiO_2 ww/CN electrode and TiO_2 /CN electrode at 0.4 $A \text{ g}^{-1}$ is shown in Fig. S12a. The TiO_2 /CN electrode exhibits a charge capacity of 224 mAh g^{-1} with initial coulombic efficiency (ICE) of 44.8%, which are much lower than those of TiO_2 ww/CN electrode. After the first cycle, the capacities of the TiO_2 ww/CN electrode increase first and then keep stable gradually. It delivers a high discharge capacity of 497 mAh g^{-1} after 1000 cycles with coulombic efficiency (CE) of nearly 100%, demonstrating excellent cyclability. Figure 3b shows the long-term cycling (6000 cycles) of the TiO_2 ww/CN electrode at 5 $A \text{ g}^{-1}$. The performance of the first 500 cycles is shown in Fig. S12b for better observation. It shows an initial discharge capacity of 401 mAh g^{-1} and an initial charge capacity of 183 mAh g^{-1} . The discharge capacity at the second cycle is 116 mAh g^{-1} , then the capacity significantly increases to 280 mAh g^{-1} at the 144th cycle. The increase may be due to the following reasons [32–36]: the activation of the electrolyte at the electrode, sectional reversible reactions of SEI, and the reversible interfacial Li-ion intercalation reactions. After that, the discharge capacity gradually increases to 367 mAh g^{-1} at nearly 4000 cycles. The TiO_2 ww/CN electrode shows an outstanding cyclability and discharge capacity as high as 303 mAh g^{-1} after 6000 cycles. Figure S12c displays the discharge/charge curves of TiO_2 ww/CN in different cycles at 0.4 $A \text{ g}^{-1}$. TiO_2 ww/CN electrode shows an initial discharge capacity of 708 mAh g^{-1} , then it shows a charge capacity of 383 mAh g^{-1} with ICE of 54%. Consistent with Fig. S12a, the large initial irreversible capacity loss is mainly in line with the solid electrolyte interphase (SEI). This may also be due to the larger specific surface area [37, 38] and the irreversible sites in Li^+ ion storage [39]. The discharge/charge profiles at subsequent cycles are overlapping well, and the coulombic efficiencies reach nearly 100%. To explore the Li-storage properties, CV and A.C. impedance of the assembled LHCs were carried out. Figure 3c is the CV curves of TiO_2 ww/CN. A pair of reduction/oxidation peaks at 1.62/2.28 V in the first scan can be ascribed to Li^+ insertion/extraction in the anatase TiO_2 [40–42]. There is a significant cathodic peak at about 0.54 V in the first cycle, which disappears in the following scans. It can be attributed to the generation of SEI film, which is formed from the irreversible reaction of electrode material

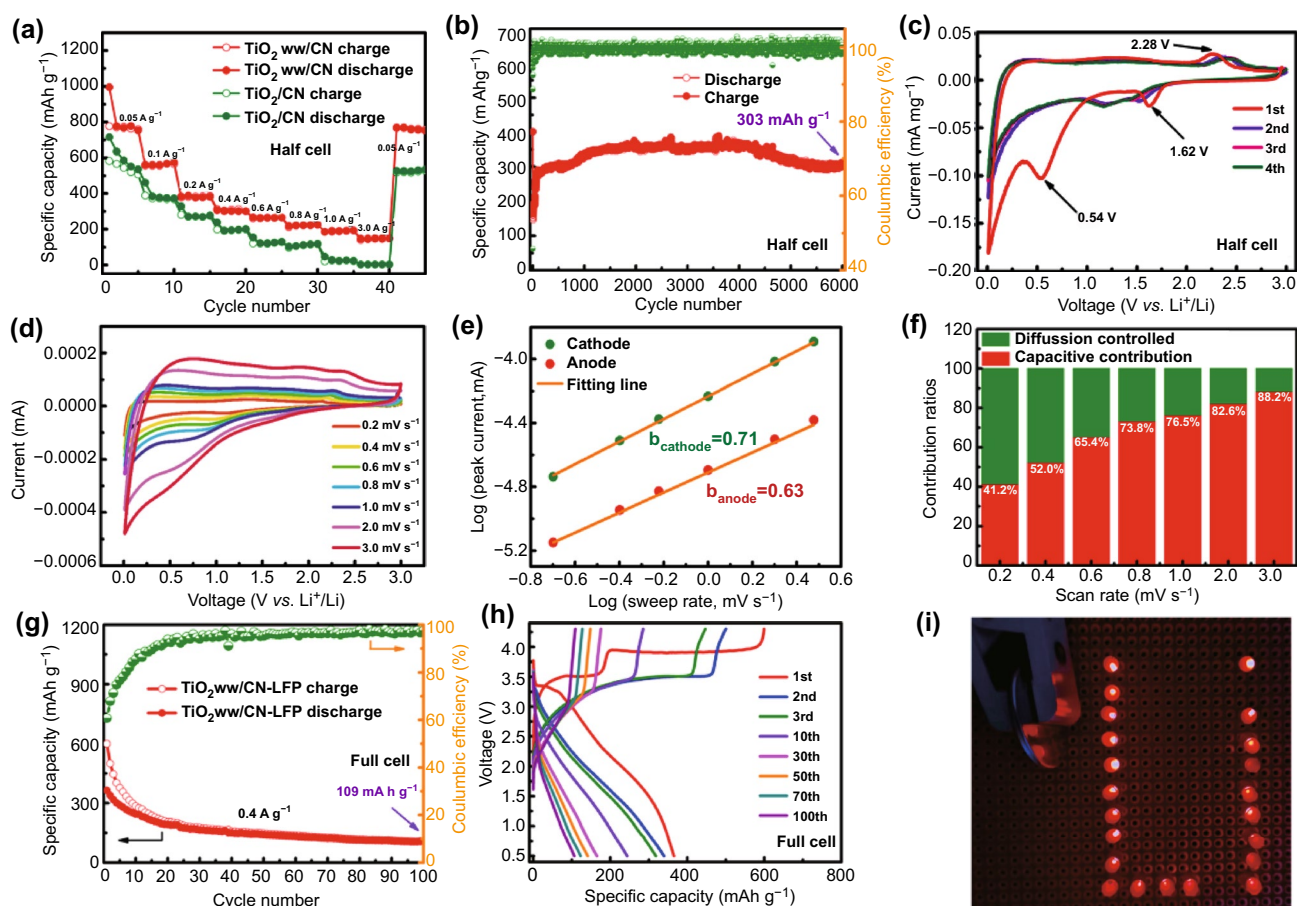


Fig. 3 TiO_2 ww/CN film and TiO_2 /CN film in LHCs: **a** rate performance at various current densities from 0.05 to 3 A g^{-1} , at last returning back to 0.05 A g^{-1} , **b** long cycling performance at 5 A g^{-1} for TiO_2 ww/CN electrode; TiO_2 ww/CN film in LHCs; **c** CV curves of TiO_2 ww/CN film at 0.1 mV s^{-1} , **d** CV curves of TiO_2 ww/CN film from 0.2 to 3.0 mV s^{-1} , **e** the log-linear relation in sweep rate \sim peak current, and **f** columnar diagram of contribution ratios from 0.2 to 3.0 mV s^{-1} ; (–) TiO_2 ww/CN-LFP(+) full cell: **g** cycling performance, and **h** corresponding discharge–charge voltage profiles at 0.4 A g^{-1} , **i** the digital picture of 22 LEDs after being lighted

and electrolyte [43–46]. After the first scan, the CV curves nearly overlapping suggesting that the TiO_2 ww/CN electrode has good electrochemical reversibility. The lithium storage performance in this work exceeds the theoretical value, thus the pseudocapacitance behavior is analyzed in Fig. 3d–f and S12d to investigate the reason. CV curves at 0.2–3.0 mV s^{-1} are explored in Fig. 3d to research the kinetic performance of the TiO_2 ww/CN electrode. In order to judge whether there is capacitive diffusion behavior in this process [11, 47, 48], the peak current (i) under the corresponding peak potential is taken to calculate from Eq. 1:

$$i = av^b \quad (1)$$

where i is the peak current, v is the scan rate, a and b are the constant. Therefore, the b value is the slope when turning Eq. 1 into a linear equation, which was shown in

Fig. 3e (b_{anode} is 0.63 and b_{cathode} is 0.71). Admittedly, b value equaled to 0.5 means diffusion-controlled and 1 means capacitive contribution. To further determine the capacitive contribution ratios, Eq. 2 is analyzed:

$$i = k_1v + k_2v^{1/2} \quad (2)$$

where k_1 and k_2 are the constant, $k_2v^{1/2}$ and k_1v correspond to diffusion and surface effects, respectively. From Fig. 3f, it's obvious that the capacitive contribution progressively increases with the increase in sweep rate and the contribution ratios of 3 mV s^{-1} is 88.2%. Figure S12d is the corresponding integral area diagram. It is speculated that the TiO_2 ww/CN electrode has better electrochemical performance in LHCs from the result of high contribution ratios. It was shown in Fig. S13 the Nyquist plots of TiO_2 ww/CN electrode and TiO_2 /CN electrode in LHCs are composed of a high-frequency semicircle, intermediate frequency

semicircle, and low-frequency straight line. The plots can be fitted according to the equivalent circuit shown as the inset in Fig. S13. The R_s is ohm resistance, R_f represents the resistance of SEI film, and R_{ct} is the resistance of charge transfer. Warburg impedance (W1) is associated with Li^+ diffusion in the solid phase. CPE1 is an analog constant-phase element that is related to the SEI film capacitor, and CPE2 is in connection with double-layer capacitance [49–51]. As shown in Table S1, TiO_2 ww/CN electrode has smaller values of R_s , R_f , and R_{ct} (1.3, 93.8, and 115.5 Ω) comparing with the TiO_2 /CN electrode (1.5, 240.0, and 405.0 Ω), indicating it possesses faster kinetics in the electrochemical reaction.

To reveal the practical application feasibility of the sample, the full cells were fabricated between activated LFP cathodes and activated TiO_2 ww/CN film anodes. The cycling performance of the LFP electrode in LHC after activating 1 cycle at 0.1 A g^{-1} (Fig. S14a) and homologous discharge/charge curves in the range of 2.5–4.3 V (Fig. S14b) manifest cyclic stability. The cycling performance of the full cell can be measured in Fig. 3g. The (–) TiO_2 ww/CN-LFP(+) full cell exhibits high coulombic efficiency of 90% after 15 cycles of activation and then possesses coulombic efficiency with 97% over 100 cycles. Laudably, it can deliver the discharge capacity and charge capacity of 109 and 106 mAh g^{-1} at the 100th cycle, respectively. The corresponding discharge/charge curves of the full cell shown in Fig. 3h can observe the explicit charging and discharging platforms even in the 100th cycle at 0.4 A g^{-1} , which indicating remarkable cycling stability. In Fig. 3i, the (–) TiO_2 ww/CN-LFP(+) full cell can glow 22 LEDs without a hitch, demonstrating the real application.

After 1000 cycles, the TiO_2 ww/CN electrode at 0.4 A g^{-1} was disassembled from the testing cell for TEM tests. The after-cycled electrode was completely soaked in dimethyl carbonate (DMC) for 8 h to remove the electrolyte residue on the film before testing. The shape of the after-cycled electrode is shown in the upper right corner of Fig. S15a. It can be observed from Fig. S15a that the wire-in-wire structure is well maintained. EDX elemental mapping image in Fig. S15b shows that the C, Ti, O elements are well distributed in the nanofibers [52]. It can be considered that the structure and morphology of the after-cycled electrode keep intact after long-term cycling. The lattice space observed in Fig. S15c is 3.5 Å, corresponding to the (101) plane of anatase, and the FFT further observed the (101) plane. To assess the electrochemical performance of the TiO_2 ww/CN electrode, this work and the other partly reported binder-free

and free-standing TiO_2 anode materials in LHCs in the recent five years are compared in Table S2. Compared with rGO modified N-doped carbon foam supporting TiO_2 [20], foam-like 3D mesopore N-doped carbon assembling TiO_2 nanoparticles [53], thick mesoporous TiO_2 films [54], and preferentially oriented TiO_2 nanotubes [55], the TiO_2 ww/CN electrode in this work has better cycling stability and higher reversible capacity. Besides, TiO_2 ww/CN also shows better cycling stability than TiO_2 layer on N-doped carbon foams [15], and TiO_2 /super-aligned C nanotube [56]. EOG/ TiO_2 (B) nanosheets [16], and N-doped TiO_2 /RGO hybrids [17] could endure extra-long term cycles of 10,000 cycles; however, TiO_2 ww/CN in this work shows advantages in the respect of specific capacity.

3.3 Electrochemical Evaluation in KHCs and Full Cells

It indicates the rate performance of the TiO_2 ww/CN electrode and the TiO_2 /CN electrode in Fig. 4a. At 0.05, 0.1, 0.2, 0.4, 0.6, 0.8, and 1 A g^{-1} , the reversible discharge capacities of TiO_2 ww/CN electrode are 222, 184, 159, 127, 106, 91, and 78 mAh g^{-1} , respectively. When backed to 0.05 A g^{-1} after 35 cycles, TiO_2 ww/CN electrode recovers the discharge capacity of 248 mAh g^{-1} . The rate capability of the TiO_2 ww/CN electrode is significantly improved than the TiO_2 /CN electrode. Figure 4b shows the cycle performance of the TiO_2 ww/CN electrode and the TiO_2 /CN electrode in KHCs at 0.05 A g^{-1} . It can be observed that the TiO_2 /CN electrode has an initial discharge capacity of 285 mAh g^{-1} , then it has an initial charge capacity of 87 mAh g^{-1} , with ICE of 30%. TiO_2 ww/CN electrode shows a much higher specific capacity and much better cyclability than the TiO_2 /CN electrode. It shows a discharge capacity of 243 mAh g^{-1} at the second cycle, and the discharge capacity increases gradually upon cycling. The discharge capacity is 258 mAh g^{-1} at the 60 cycles. After 1000 cycles, the discharge capacity of 259 mAh g^{-1} could be obtained with coulombic efficiencies of nearly 100%. The discharge/charge curves of the TiO_2 ww/CN electrode at 0.05 A g^{-1} are shown in Fig. 4c. What can be observed is, the initial discharge capacity reaches 608 mAh g^{-1} and the initial charge capacity is 219 mAh g^{-1} ; therefore, it can be calculated that the ICE is 36%. The second, the third, and the tenth curves have unexceptionable repetition, which proves the outstanding cycling stability. The K-storage performances of the TiO_2 ww/CN



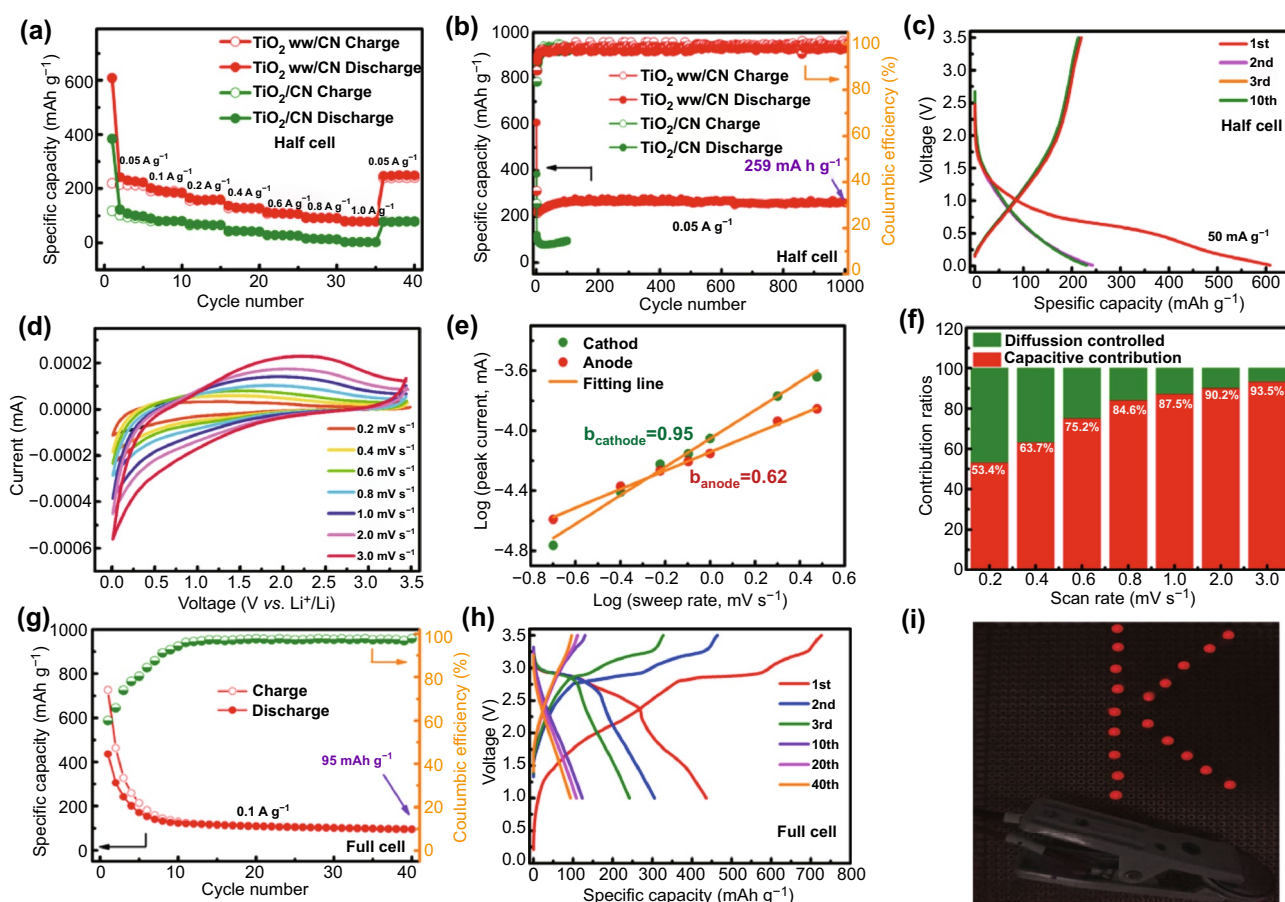


Fig. 4 TiO_2 ww/CN film and TiO_2/CN film in KHCs: **a** rate performance from 0.05 to 1.0 A g^{-1} , then returning back to 0.05 A g^{-1} , **b** cycle performance at 0.05 A g^{-1} ; TiO_2 ww/CN film in KHCs: **c** discharge-charge voltage profiles of TiO_2 ww/CN film at 0.05 A g^{-1} , **d** CV curves of TiO_2 ww/CN film electrode from 0.2 to 3.0 mV s^{-1} , **e** the log-linear relation in sweep rate ~ peak current, and **f** columnar diagram of contribution ratios from 0.2 to 3.0 mV s^{-1} ; (-) TiO_2 ww/CN-PTCDA(+) full cell: **g** cycling performance, and **h** corresponding discharge-charge voltage profiles at 0.1 A g^{-1} , **i** the digital picture of 19 LEDs after being lighted

film electrode are also investigated. KHCs have the same working mechanism as LHCs and approximate standard reduction potential compared with LHCs; however, there is a huge difference in energy storage capacity between LHCs and KHCs. DFT calculations were carried out to reveal the intrinsic property of TiO_2 when utilized as the electrode of LHCs and KHCs. The total density of states (TDOS) of dilute Li/K intercalated TiO_2 is shown in Fig. S16a. It can be found that the alkali metal ions can generate intermediate states in the bandgap, which are slightly lower than the Fermi level. The gap between the intermediate states and conduction band is around 1.2 eV, suggesting that both the Li and K ion intercalated TiO_2 have relatively good electronic conductivity. However, for the ionic diffusion barrier of Li/K ions in anatase TiO_2 (1 Li/K atom intercalated in a $(2 \times 2 \times 3)$

supercell), as previously revealed by us [29], the diffusion of K^+ ions in TiO_2 has a much larger kinetic barrier (0.70 eV) than that of Li^+ ions (0.34 eV), which is indicative of the sluggish reaction kinetics of TiO_2 as the electrode of KHCs. In consequence, it can conclude that the reaction of TiO_2 in KHCs is primarily restricted by the ionic conductivity, which could be significantly improved by reducing the particle size of TiO_2 . Figure S16b shows CV curves from the first to three cycles of TiO_2 ww/CN in 0.01–3.5 V (V vs. K^+/K) at 0.1 mV s^{-1} . The obvious cathodic peak at 0.2 V in the first scan is mainly attributed to the formation of SEI film. The 3.5–1.15 V of the cathodic process and the 2.28–3.5 V of the anodic process are the K^+ adsorption/deadsorption, corresponding to the pseudo-capacitive effect [18]. The 1.15–0.01 V of the cathodic process and the 0.01–2.28 V of

the anodic process are the K^+ intercalation/deintercalation [18]. The area surrounded by the CV curve in the third scan is slightly larger than that in the second scan, indicating the electrochemical activation in the first few cycles. Similar to TiO_2 ww/CN electrode in LHCs, capacitive contribution in KHCs is shown in Figs. 4d–f and S16c referencing to Eqs. 1 and 2. Under the influence of ohmic impedance and polarization, CV curves (in Fig. 4d) are gradually distorted from 0.2 mV s^{-1} to 3.0 mV s^{-1} . It can be seen from Fig. 4e that b_{anode} values (0.62) in KHCs are close to b_{anode} values (0.63) in LHCs; however, b_{cathode} values (0.95) in KHCs is extremely higher than b_{anode} values (0.71) in LHCs. The contribution ratios in varying sweep speed and corresponding integral area curve in 3.0 mV s^{-1} are described in Fig. 4f and S16c, respectively. It notes that the capacitive contribution ratios of the TiO_2 ww/CN electrode in KHCs are larger than those in LHCs. For example, the capacitive contribution ratio in KHCs is as high as 93.5% at 3.0 mV s^{-1} , which is larger than that in LHCs (88.2%). Despite the large diffusion barrier of K in anatase TiO_2 (0.70 eV) [29], TiO_2 ww/CN film shows attractive K-storage performance, which could be in keeping with the pseudocapacitance contribution and large specific surface area.

The cycling performance at 0.1 A g^{-1} (Fig. S17a) and corresponding discharge/charge curves (Fig. S17b) in 1.5–3.5 V of PTCDA in KHC demonstrate that it has good cycle stability and obvious charging/discharging platforms. The cycling performance (Fig. 4g) and corresponding discharge/charge curves (Fig. 4h) of $(-)/TiO_2$ ww/CN-PTCDA $(+)$ full cells also display high storage capacity and outstanding cycling stability. It could deliver initial charge/discharge capacities of 726/435 mAh g^{-1} with a coulombic efficiency of 60% at 0.1 A g^{-1} , after 8 cycles of activation, the coulombic efficiency gradually approached 90%. At last, the charge/discharge capacities can be maintained at 95/93 mAh g^{-1} over 40 cycles with a coulombic efficiency of 97% (Fig. 4g), showing a high storage capacity. The unambiguous charging/discharging platforms even after 40 cycles in Fig. 4h further demonstrate its excellent cyclic stability. Desirably, the 100% charged $(-)/TiO_2$ ww/CN-PTCDA $(+)$ full cell can allow the 19 LEDs light shine (Fig. 4i).

The TiO_2 ww/CN electrode after 1000 cycles in KHCs at 0.05 A g^{-1} was taken apart and washed with dimethyl carbonate for TEM tests. The digital photo shown as the inset in Fig. S18a indicates that the TiO_2 ww/CN film is intact after 1000 cycles. Figure S18a shows the wire-in-wire

hierarchical structure of nanofibers remains well and the surface is slightly rough which may be caused by the formation of SEI film. The EDX elemental mapping images in Fig. S18b shows that K, C, Ti, O elements are well distributed in the fiber. As shown in the HRTEM image (Fig. S18c), the lattice fringes space and the FFT are all 3.5 \AA , corresponding to the (101) crystal plane of anatase TiO_2 . The comparison results of this work with previous reported TiO_2 anode materials in KHCs are listed in Table S3. This work shows better cycling stability than lepidocrocite-type layered TiO_2 and MXene-derived TiO_2 /RGO [19, 20]. Hierarchical TiO_2 -C micro-tubes [18] could deliver 133 mAh g^{-1} after 1200 cycles at 0.5 A g^{-1} , which showed outstanding electrochemical properties. It notes that the TiO_2 ww/CN electrode in this work is a binder-free and free-standing electrode, demonstrating commendable mechanical flexibility.

4 Conclusions

In this work, electrospun TiO_2 ww/CN film with a unique hierarchical wire-in-wire nanostructure and excellent mechanical flexibility was fabricated. As free-standing electrodes, the film demonstrated highly improved electrochemical performance in Li/K ion batteries. It delivered discharge capacities of 497 mAh g^{-1} after 1000 cycles at 0.4 A g^{-1} and 303 mAh g^{-1} after 6000 cycles at 5 A g^{-1} in Li half-cells, and a discharge capacity of 259 mAh g^{-1} at 0.05 A g^{-1} after 1000 cycles in K half-cells. Despite the large K^+ ions diffusion barrier in TiO_2 , the K-ion storage performance of TiO_2 ww/CN was found to be enhanced by the high pseudocapacitance contribution (93.5% under 3.0 mV s^{-1}). When TiO_2 ww/CN film was directly used as anodes and matched with corresponding cathodes (LFP or PTCDA) to assemble the full cells, it showed high discharge capacities, excellent cyclic stability, and attractive practical application (lighting more than 19 LEDs at least). Therefore, TiO_2 ww/CN film has broad application prospects as anode materials for LIBs and KIBs.

Acknowledgments This work was supported financially by the National Natural Science Foundation of China (Grant Nos. 51672234, 52072325), the Key Research Foundation of Education Bureau of Hunan Province, China (Grant No. 20A486), Hunan 2011 Collaborative Innovation Center of Chemical Engineering and Technology with Environmental Benignity and Effective Resource Utilization, Program for Innovative Research Cultivation Team in University of Ministry of Education of China (1337304),

and the 111 Project (B12015). Computational resources provided by the National Supercomputing Center in Changsha are gratefully acknowledged.

Open Access This article is licensed under a Creative Commons Attribution 4.0 International License, which permits use, sharing, adaptation, distribution and reproduction in any medium or format, as long as you give appropriate credit to the original author(s) and the source, provide a link to the Creative Commons licence, and indicate if changes were made. The images or other third party material in this article are included in the article's Creative Commons licence, unless indicated otherwise in a credit line to the material. If material is not included in the article's Creative Commons licence and your intended use is not permitted by statutory regulation or exceeds the permitted use, you will need to obtain permission directly from the copyright holder. To view a copy of this licence, visit <http://creativecommons.org/licenses/by/4.0/>.

Supplementary Information The online version contains supplementary material available at <https://doi.org/10.1007/s40820-021-00632-4>.

References

1. C. Lu, Z. Sun, L. Yu, X. Lian, Y. Yi et al., Enhanced kinetics harvested in heteroatom dual-doped graphitic hollow architectures toward high rate printable potassium-ion batteries. *Adv. Energy Mater.* **10**, 2001161 (2020). <https://doi.org/10.1002/aenm.202001161>
2. Y. Zhang, Y. Ouyang, L. Liu, J. Xia, S. Nie et al., Synthesis and characterization of $\text{Na}_{0.44}\text{MnO}_2$ nanorods/graphene composite as cathode materials for sodium-ion batteries. *J. Cent. South Univ.* **26**, 1510–1520 (2019). <https://doi.org/10.1007/s11771-019-4107-6>
3. R. Guo, X. Liu, B. Wen, F. Liu, J. Meng et al., Engineering mesoporous structure in amorphous carbon boosts potassium storage with high initial coulombic efficiency. *Nano-Micro Lett.* **12**, 148 (2020). <https://doi.org/10.1007/s40820-020-00481-7>
4. J. Wang, L. Fan, Z. Liu, S. Chen, Q. Zhang et al., In situ alloying strategy for exceptional potassium ion batteries. *ACS Nano* **13**, 3703–3713 (2019). <https://doi.org/10.1021/acsnano.9b00634>
5. L. Fan, R. Ma, J. Wang, H. Yang, B. Lu, An ultrafast and highly stable potassium-organic battery. *Adv. Mater.* **30**, 1805486 (2018). <https://doi.org/10.1021/acsnano.9b00634>
6. J. Xia, L. Liu, S. Jamil, J. Xie, H. Yan et al., Free-standing SnS/C nanofiber anodes for ultralong cycle-life lithium-ion batteries and sodium-ion batteries. *Energy Storage Mater.* **17**, 1–11 (2019). <https://doi.org/10.1016/j.ensm.2018.08.005>
7. L. Wang, G. Yang, J. Wang, S. Wang, C. Wang et al., In situ fabrication of branched TiO_2/C nanofibers as binder-free and free-standing anodes for high-performance sodium-ion batteries. *Small* **15**, 1901584 (2019). <https://doi.org/10.1002/sml.201901584>
8. W.-C. Chang, J.-H. Wu, K.-T. Chen, H.-Y. Tuan, Red phosphorus potassium-ion battery anodes. *Adv. Sci.* **6**, 1801354 (2019). <https://doi.org/10.1002/adv.201801354>
9. I. Sultana, M.M. Rahman, T. Ramireddy, Y. Chen, A.M. Glushenkov, High capacity potassium-ion battery anodes based on black phosphorus. *J. Mater. Chem. A* **5**, 23506–23512 (2017). <https://doi.org/10.1039/c7ta02483e>
10. H. Luo, M. Chen, J. Cao, M. Zhang, S. Tan et al., Cocoon silk-derived, hierarchically porous carbon as anode for highly robust potassium-ion hybrid capacitors. *Nano-Micro Lett.* **12**, 113 (2020). <https://doi.org/10.1007/s40820-020-00454-w>
11. S. Nie, L. Liu, J. Liu, J. Xie, Y. Zhang et al., Nitrogen-doped $\text{TiO}_2\text{-C}$ composite nanofibers with high-capacity and long-cycle life as anode materials for sodium-ion batteries. *Nano-Micro Lett.* **10**, 71 (2018). <https://doi.org/10.1007/s40820-018-0225-1>
12. S. Rehman, J. Liu, Z. Fang, J. Wang, R. Ahmed et al., Heterostructured $\text{TiO}_2/\text{C}/\text{Co}$ from ZIF-67 frameworks for microwave-absorbing nanomaterials. *ACS Appl. Nano Mater.* **2**, 4451–4461 (2019). <https://doi.org/10.1021/acsnano.9b00841>
13. S. Nie, L. Liu, J. Liu, J. Xia, Y. Zhang et al., $\text{TiO}_2\text{-Sn/C}$ composite nanofibers with high-capacity and long-cycle life as anode materials for sodium ion batteries. *J. Alloys Compd.* **772**, 314–323 (2019). <https://doi.org/10.1016/j.jallcom.2018.09.044>
14. S. Huang, L. Zhang, X. Lu, L. Liu, X. Liu et al., Tunable pseudocapacitance in 3D $\text{TiO}_2\text{-}\delta$ nanomembranes enabling superior lithium storage performance. *ACS Nano* **11**, 821–830 (2017). <https://doi.org/10.1021/acsnano.6b07274>
15. S. Chu, Y. Zhong, R. Cai, Z. Zhang, S. Wei et al., Mesoporous and nanostructured TiO_2 layer with ultra-high loading on nitrogen-doped carbon foams as flexible and free-standing electrodes for lithium-ion batteries. *Small* **12**, 6724–6734 (2016). <https://doi.org/10.1002/sml.201602179>
16. G. Ren, M. Hoque, J. Liu, J. Warzywoda, Z. Fan, Perpendicular edge oriented graphene foam supporting orthogonal $\text{TiO}_2(\text{B})$ nanosheets as freestanding electrode for lithium ion battery. *Nano Energy* **21**, 162–171 (2016). <https://doi.org/10.1016/j.nanoen.2016.01.010>
17. Y. Shi, D. Yang, R. Yu, Y. Liu, J. Qu et al., Efficient photocatalytic reduction approach for synthesizing chemically bonded N-doped TiO_2 /reduced graphene oxide hybrid as a freestanding electrode for high-performance Lithium storage. *ACS Appl. Energy Mater.* **1**, 4186–4195 (2018). <https://doi.org/10.1021/acsaem.8b00836>
18. Y. Li, C. Yang, F. Zheng, Q. Pan, Y. Liu et al., Design of TiO_2/C hierarchical tubular heterostructures for high performance potassium ion batteries. *Nano Energy* **59**, 582–590 (2019). <https://doi.org/10.1016/j.nanoen.2019.03.002>
19. K.G. Reeves, J. Ma, M. Fukunishi, M. Salanne, S. Komaba et al., Insights into Li^+ , Na^+ , and K^+ intercalation in lepidocrocite-type layered TiO_2 structures. *ACS Appl. Energy Mater.* **1**, 2078–2086 (2018). <https://doi.org/10.1021/acsaem.8b00170>

20. Y. Fang, R. Hu, B. Liu, Y. Zhang, K. Zhu et al., MXene-derived TiO₂/reduced graphene oxide composite with an enhanced capacitive capacity for Li-ion and K-ion batteries. *J. Mater. Chem. A* **7**, 5363–5372 (2019). <https://doi.org/10.1039/c8ta12069b>
21. G. Kresse, J. Hafner, Ab initio molecular dynamics for open-shell transition metals. *Phys. Rev. B* **48**, 13115–13118 (1993). <https://doi.org/10.1103/PhysRevB.48.13115>
22. G. Kresse, J. Furthmuller, Efficiency of ab-initio total energy calculations for metals and semiconductors using a plane-wave basis set. *Comput. Mater. Sci.* **6**, 15–50 (1996). [https://doi.org/10.1016/0927-0256\(96\)00008-0](https://doi.org/10.1016/0927-0256(96)00008-0)
23. P.E. Blochl, Projector augmented-wave method. *Phys. Rev. B* **50**, 17953–17979 (1994). <https://doi.org/10.1103/PhysRevB.50.17953>
24. J.P. Perdew, K. Burke, M. Ernzerhof, Generalized gradient approximation made simple. *Phys. Rev. Lett.* **77**, 3865–3868 (1996). <https://doi.org/10.1103/PhysRevLett.77.3865>
25. L. Shao, S. Quan, Y. Liu, Z. Guo, Z. Wang, A novel “gel-sol” strategy to synthesize TiO₂ nanorod combining reduced graphene oxide composites. *Mater. Lett.* **107**, 307–310 (2013). <https://doi.org/10.1016/j.matlet.2013.06.050>
26. Y.-L. Huang, S.-M. Yuen, C.-C.M. Ma, C.-Y. Chuang, K.-C. Yu et al., Morphological, electrical, electromagnetic interference (EMI) shielding, and tribological properties of functionalized multi-walled carbon nanotube/poly methyl methacrylate (PMMA) composites. *Compos. Sci. Technol.* **69**, 1991–1996 (2009). <https://doi.org/10.1016/j.compscitech.2009.05.006>
27. H. Wang, Q. Wu, D. Cao, X. Lu, J. Wang et al., Synthesis of SnSb-embedded carbon-silica fibers via electrospinning: effect of TEOS on structural evolutions and electrochemical properties. *Mater. Today Energy* **1**, 24–32 (2016). <https://doi.org/10.1016/j.compscitech.2009.05.006>
28. X. Lu, H. Wang, Z. Wang, Y. Jiang, D. Cao et al., Room-temperature synthesis of colloidal SnO₂ quantum dot solution and ex-situ deposition on carbon nanotubes as anode materials for lithium ion batteries. *J. Alloys Compd.* **680**, 109–115 (2016). <https://doi.org/10.1016/j.jallcom.2016.04.128>
29. D. Su, L. Liu, Z. Liu, J. Dai, J. Wen et al., Electrospun Ta-doped TiO₂/C nanofibers as high-capacity and long-cycling anode materials for Li-ion and K-ion batteries. *J. Mater. Chem. A* **8**, 20666–20676 (2020). <https://doi.org/10.1039/D0TA06327D>
30. H. Fan, H. Yu, Y. Zhang, J. Guo, Z. Wang et al., 1D to 3D hierarchical iron selenide hollow nanocubes assembled from FeSe₂@C core-shell nanorods for advanced sodium ion batteries. *Energy Storage Mater.* **10**, 48–55 (2018). <https://doi.org/10.1016/j.ensm.2017.08.006>
31. H. Lin, M. Li, X. Yang, D. Yu, Y. Zeng et al., Nanosheets-assembled CuSe crystal pillar as a stable and high-power anode for sodium-ion and potassium-ion batteries. *Adv. Energy Mater.* **9**, 1900323 (2019). <https://doi.org/10.1002/aenm.201900323>
32. D. Su, J. Liu, Y. Pei, L. Liu, S. Nie et al., Electrospun Na doped Li₂TiSiO₅/C nanofibers with outstanding lithium-storage performance. *Appl. Surf. Sci.* **541**, 148388 (2021). <https://doi.org/10.1016/j.apsusc.2020.148388>
33. L. Su, J. Hei, X. Wu, L. Wang, Z. Zhou, Ultrathin layered hydroxide cobalt acetate nanoplates face-to-face anchored to graphene nanosheets for high-efficiency lithium storage. *Adv. Funct. Mater.* **27**, 1605544 (2017). <https://doi.org/10.1002/adfm.201605544>
34. J. Liu, D. Su, L. Liu, Z. Liu, S. Nie et al., Boosting the charge transfer of Li₂TiSiO₅ using nitrogen-doped carbon nanofibers: towards high-rate, long-life lithium-ion batteries. *Nanoscale* **12**, 19702–19710 (2020). <https://doi.org/10.1039/d0nr04618c>
35. D. Ying, R. Ding, Y. Huang, W. Shi, Q. Xu et al., An intercalation pseudocapacitance-driven perovskite NaNbO₃ anode with superior kinetics and stability for advanced lithium-based dual-ion batteries. *J. Mater. Chem. A* **7**, 18257–18266 (2019). <https://doi.org/10.1039/C9TA06438A>
36. Q. Xu, R. Ding, W. Shi, D. Ying, Y. Huang et al., Perovskite KNi_{0.1}Co_{0.9}F₃ as a pseudocapacitive conversion anode for high-performance nonaqueous Li-ion capacitors and dual-ion batteries. *J. Mater. Chem. A* **7**, 8315–8326 (2019). <https://doi.org/10.1039/C9TA00493A>
37. H. Yang, R. Xu, Y. Gong, Y. Yao, L. Gu et al., An interpenetrating 3D porous reticular Nb₂O₅@carbon thin film for superior sodium storage. *Nano Energy* **48**, 448–455 (2018). <https://doi.org/10.1016/j.nanoen.2018.04.006>
38. J. Ni, W. Wang, C. Wu, H. Liang, J. Maier et al., Energy storage: highly reversible and durable Na storage in niobium pentoxide through optimizing structure, composition, and nano-architecture. *Adv. Mater.* **29**, 1605607 (2017). <https://doi.org/10.1002/adma.201770063>
39. X. Yan, Y. Li, M. Li, Y. Jin, F. Du et al., Ultrafast lithium storage in TiO₂-bronze nanowires/N-doped graphene nanocomposites. *J. Mater. Chem. A* **3**, 4180–4187 (2015). <https://doi.org/10.1039/C4TA06361A>
40. Y. Jiang, S. Chen, D. Mu, Z. Zhao, C. Li et al., Flexible TiO₂/SiO₂/C film anodes for lithium-ion batteries. *Chemosuschem* **11**, 2040–2044 (2018). <https://doi.org/10.1002/cssc.201800560>
41. Y. Yue, D. Juarez-Robles, Y. Chen, L. Ma, W.C. Kuo et al., Hierarchical structured Cu/Ni/TiO₂ nanocomposites as electrodes for lithium-ion batteries. *ACS Appl. Mater. Interfaces* **9**, 28695–28703 (2017). <https://doi.org/10.1021/acsami.7b10158>
42. C. Zhang, S. Liu, Y. Qi, F. Cui, X. Yang, Conformal carbon coated TiO₂ aerogel as superior anode for lithium-ion batteries. *Chem. Eng. J.* **351**, 825–831 (2018). <https://doi.org/10.1016/j.cej.2018.06.125>
43. S. Anwer, Y. Huang, J. Liu, J. Liu, M. Xu et al., Nature-inspired Na₂Ti₃O₇ nanosheets-formed three-dimensional microflowers architecture as a high-performance anode material for rechargeable sodium-ion batteries. *ACS Appl. Mater. Interfaces* **9**, 11669–11677 (2017). <https://doi.org/10.1021/acsami.7b01519>
44. D. Xu, C. Chen, J. Xie, A hierarchical N/S-codoped carbon anode fabricated facilely from cellulose/polyaniline microspheres for high-performance sodium-ion batteries. *Adv.*



- Energy Mater. **6**, 1501929 (2016). <https://doi.org/10.1002/aenm.201501929>
45. E. Liu, J. Wang, C. Shi, N. Zhao, C. He et al., Anomalous interfacial lithium storage in graphene/TiO₂ for lithium ion batteries. *ACS Appl. Mater. Interfaces* **6**, 18147–18151 (2014). <https://doi.org/10.1021/am5050423>
 46. Z. Bi, M.P. Paranthaman, B. Guo, R.R. Unocic, H.M. Meyer III et al., High performance Cr, N-codoped mesoporous TiO₂ microspheres for lithium-ion batteries. *J. Mater. Chem. A* **2**, 1818–1824 (2014). <https://doi.org/10.1039/c3ta14535b>
 47. Y. Li, Y. Huang, Y. Zheng, R. Huang, J. Yao, Facile and efficient synthesis of α -Fe₂O₃ nanocrystals by glucose-assisted thermal decomposition method and its application in lithium ion batteries. *J. Power Sources* **416**, 62–71 (2019). <https://doi.org/10.1016/j.jpowsour.2019.01.080>
 48. J. Sun, L. Guo, X. Sun, J. Zhang, L. Hou et al., One-dimensional nanostructured pseudocapacitive materials: design, synthesis and applications in supercapacitors. *Batteries Supercaps* **2**, 820–841 (2019). <https://doi.org/10.1002/batt.201900021>
 49. C. Wang, J. Zhang, X. Wang, C. Lin, X. Zhao, Hollow rutile cuboid arrays grown on carbon fiber cloth as a flexible electrode for sodium-ion batteries. *Adv. Funct. Mater.* **30**, 2002629 (2020). <https://doi.org/10.1002/adfm.202002629>
 50. C. Wang, X. Wang, C. Lin, X. Zhao, Lithium titanate cuboid arrays grown on carbon fiber cloth for high-rate flexible Lithium-ion batteries. *Small* **15**, 1902183 (2019). <https://doi.org/10.1002/sml.201902183>
 51. C. Wang, X. Wang, C. Lin, S. Xiu, Spherical vanadium phosphate particles grown on carbon fiber cloth as flexible anode for high-rate Li-ion batteries. *Chem. Eng. J.* **15**, 123981 (2020). <https://doi.org/10.1016/j.cej.2019.123981>
 52. Z. Wang, J. Sha, E. Liu, C. He, C. Shi et al., A large ultrathin anatase TiO₂ nanosheet/reduced graphene oxide composite with enhanced lithium storage capability. *J. Mater. Chem. A* **2**, 8893–8901 (2014). <https://doi.org/10.1039/c4ta00574k>
 53. Y. Yuan, F. Chen, S. Yin, L. Wang, M. Zhu et al., Foam-like, 3-dimension mesoporous N-doped carbon-assembling TiO₂ nanoparticles (P25) as high-performance anode material for lithium-ion batteries. *J. Power Sources* **420**, 38–45 (2019). <https://doi.org/10.1016/j.jpowsour.2019.02.094>
 54. N.Ž Knežević, E. Ruiz-Hernández, W.E. Hennink, M. Vallet-Regí, Magnetic mesoporous silica-based core/shell nanoparticles for biomedical applications. *RSC Adv.* **3**, 9584–9593 (2013). <https://doi.org/10.1039/c3ra23127e>
 55. A. Auer, E. Portenkirchner, T. Götsch, C. Valero-Vidal, S. Penne et al., Preferentially oriented TiO₂ nanotubes as anode material for Li-ion batteries: insight into Li-ion storage and Lithiation kinetics. *ACS Appl. Mater. Interfaces* **9**, 36828–36836 (2017). <https://doi.org/10.1021/acsami.7b11388>
 56. K. Zhu, Y. Luo, F. Zhao, J. Hou, X. Wang et al., Free-standing, binder-free titania/super-aligned carbon nanotube anodes for flexible and fast-charging Li-ion batteries. *ACS Sustain. Chem. Eng.* **6**, 3426–3433 (2018). <https://doi.org/10.1021/acssuschemeng.7b03671>